3D structure of eukaryotic flagella in a quiescent state revealed by cryo-electron tomography

Daniela Nicastro*†, J. Richard McIntosh‡§, and Wolfgang Baumeister*

*Abteilung Molekulare Strukturbiologie, Max-Planck-Institut für Biochemie, 82152 Martinsried, Germany; and ‡Laboratory for 3D Electron Microscopy of Cells, Department of Molecular, Cellular, and Developmental Biology, UCB 347, University of Colorado, Boulder, CO 80309

Contributed by J. Richard McIntosh, September 21, 2005

We have used cryo-electron tomography to investigate the 3D structure and macromolecular organization of intact, frozen-hydrated sea urchin sperm flagella in a quiescent state. The tomographic reconstructions provide information at a resolution better than 6 nm about the *in situ* arrangements of macromolecules that are key for flagellar motility. We have visualized the heptameric rings of the motor domains in the outer dynein arm complex and determined that they lie parallel to the plane that contains the axes of neighboring flagellar microtubules. Both the material associated with the central pair of microtubules and the radial spokes display a plane of symmetry that helps to explain the planar beat pattern of these flagella. Cryo-electron tomography has proven to be a powerful technique for helping us understand the relationships between flagellar structure and function and the design of macromolecular machines *in situ*.

axoneme | dynein | microtubule | motility | sperm

Eukaryotic cilia and flagella are highly ordered organelles that are used by a great variety of species and cell types to generate motion. Despite the diversity of their motile functions, the basic architecture of these machines is remarkably conserved (for review, see ref. 1). All such structures are built on an ordered assembly of microtubules known as the axoneme. The most widely distributed form of the axoneme consists of nine outer microtubule doublets (MTDs) and two singlet microtubules (2, 3). The combination of many structural and enzymatic studies with *in vitro* motility assays and computer-based simulations has laid a framework for our understanding about how flagellar motion is generated. Sliding between pairs of outer MTDs is powered by the dynein ATPases and converted into flagellar bending as a result of constraints imposed on interdoublet sliding by protein cross-links, such as nexin, which lie between adjacent MTDs (for reviews, see refs. 4 and 5). For an axoneme to generate the complex motions typical of beating cilia and flagella, there must be precise control of dynein's action, both around the circumference and along the length of the axoneme.

Because of their biological and medical importance and their utility as a model for other forms of microtubule-based motility (6), flagella and cilia have been studied extensively (for reviews, see refs. 3, 5, and 7–9). However, despite the increase in knowledge about isolated components of the axoneme, much remains to be learned about the mechanical and regulatory mechanisms underlying flagellar motion (3, 10). To elucidate the role of all of the players in axoneme motility, one will need a better understanding of the organization of axonemal elements *in situ* at a resolution that will characterize the structural changes that they undergo during functional cycles.

Sea urchin sperm tails are an admirable material for this sort of study because they are built with a classic "9 + 2" axoneme, and their beat pattern is mainly planar, greatly simplifying the geometry of their function in comparison with flagella with more complex beats. Murray (11) showed that rapid freezing of sea urchin sperm flagella retains structural features to a resolution of ≈3 nm. However, in 2D projection images of whole flagella, most structural details were obscured by the effects of superposition. McEwen *et al.* (12) have used electron tomography (ET) to study chemically fixed and resin-embedded cilia from newt lung. ET uses 2D projection images from many different viewing angles to reconstruct an object in three dimensions (13, 14). These researchers were able to identify major features of axonemes in the tomographic reconstructions of the 250-nm-thick sections, but at a resolution of ≈12 nm, detailed insights into the molecular organization of the axoneme were not available.

Thanks to technological advances of the past decade, ET can now be applied to relatively large, frozen-hydrated structures. Our approach has been to use ET of frozen-hydrated spermatozoa to produce 3D maps at good spatial resolution (5–8 nm). These maps allow visualization of the molecular details of flagellar structure while the organelle is preserved in an essentially native state, thanks to the properties of rapid freezing (15, 16). In this study, we have used quiescent sea urchin sperm flagella. The relatively small diameter of these flagella (≈260 nm) has allowed us to obtain tomograms that show strong diffraction over a wide range of spatial frequencies. In addition, the use of inactive flagella with long segments that are nearly straight has facilitated image analysis and 3D correlation averaging of periodic features along the axoneme, which significantly improves the image signal-to-noise ratio. Moreover, because the motor proteins of these samples are inactive, they are likely to be in the same structural conformation, making their average structures particularly informative. As a result, we can better visualize the structural features of these flagella and characterize several of the important players involved in flagellar motility. Our 3D maps not only show features of the dynein motor domain *in situ* that have previously been seen only in isolated material but also reveal previously uncharacterized aspects of the organization of the dynein arms, radial spokes, and material associated with the central microtubules.

Materials and Methods

Sample Preparation. Sea urchins (*Arbacia lixula*) were collected at the Mediterranean Sea when needed and kept in the laboratory at room temperature for up to 3 weeks in artificial seawater. Spawning was induced by injection of 1–2 ml of 0.5 M KCl into the perivisceral cavity (17). Sperm samples were collected and kept on ice without dilution in seawater to prevent sperm activation (18). Grids covered with a holey carbon film (Quantifoil, Jena, Germany) were glow-discharged and then treated with a suspension containing 10-nm colloidal gold particles (Sigma) and air-dried. Within 1 h after spawning, a few microliters of unfixed and unstained sperm cells were applied to a grid.

Conflict of interest statement: No conflicts declared.

Abbreviations: CPC, central pair complex; ET, electron tomography; IDA, inner dynein arm; MTD, microtubule doublet; ODA, outer dynein arm.

†To whom correspondence may be sent at the present address: Laboratory for 3D Electron Microscopy of Cells, Department of Molecular, Cellular, and Developmental Biology, UCB 347, University of Colorado, Boulder, CO 80309. E-mail: nicastro@colorado.edu.

§To whom correspondence may be addressed. E-mail: richard.mcintosh@colorado.edu.

© 2005 by The National Academy of Sciences of the USA

After blotting excess fluid with filter paper, we plunged the grid into liquid ethane (16). The vitrified sample was then immediately transferred into a liquid nitrogen dewar for storage.

Electron Microscopy. The sample was transferred under liquid nitrogen to a ±70° cryo-tilt holder (Gatan, Pleasanton, CA), and a total of 13 tilt series were recorded by using a CM300 transmission electron microscope (FEI, Eindhoven, The Netherlands) equipped with a field emission gun and operated at an acceleration voltage of 300 kV. The specimen was tilted about one axis with 1° or 1.5° increments over a total angular range of ≈−65° to +65°. To minimize the electron dose applied to the ice-embedded specimen, data were recorded under low-dose conditions by using automated data acquisition software (14). The total dose accumulated during the tilt series was kept at <100 electrons per Å^2. The microscope was equipped with a Gatan postcolumn energy filter (GIF 2002) that was operated in the zero-energy-loss mode with a slit width of 20 eV. To account for the increased specimen thickness at high-tilt angles, the exposure time was multiplied by a factor of $1/\cos\alpha$ (where α = tilt angle). The recording device was a 2,048 × 2,048-pixel charge-coupled device camera (Gatan). The pixel size in unbinned images was 0.82 or 0.59 nm, depending on the chosen microscope magnification. Images were recorded 3–6 μm under focus to enhance contrast. Under these conditions, the contrast transfer function has its first zero before contrast reversals at spatial frequencies between 2.4 and 3.4 nm^{-1}. Because this frequency is lower than the resolution in our reconstructions, a correction for defocus has been unnecessary.

Image Processing. All 2D projection images of a tilt series were aligned with respect to a common origin by using 10-nm colloidal gold particles as fiducial markers. 3D reconstructions were calculated by weighted back-projection. Axonemes are periodic structures and therefore contain multiple copies of equivalent particles. However, they are not truly crystalline, so broad brush averaging by Fourier methods can average out important details and local differences. This situation motivated the application of 3D correlation averaging methods to improve the image signal-to-noise ratio and thus the resolution. For this approach, apparently equivalent particles were cut from the tomograms and aligned with respect to one another, and their volumes were averaged. Only particles along one MTD of straight axonemes were included in each average, so compensation for the missing wedge was unnecessary. All computations were carried out by using the software package EM PROGRAM (19, 20). For visualization, surface and volume rendering was provided by the AMIRA 3D visualization package (Mercury Computer Systems, San Diego). In the case of the surface-rendered representation of the whole flagellum (Fig. 2), translational shift averaging and a nonlinear anisotropic diffusion algorithm (21) were applied to reduce noise before visualization. Unless otherwise stated, all surface and volume rendering was done without manual contouring or feature enhancement. For modeling the location of the radial spokes (Fig. 3 *g–k*), we used the IMOD software package (22).

Results

3D Organization of Frozen-Hydrated Flagella. Several single-axis tilt series of quiescent, frozen-hydrated flagella were recorded and reconstructed. Although 2D projection images of sea urchin sperm flagella in vitreous ice are relatively indistinct (Fig. 1*a*), tomographic reconstructions of the same structures clearly reveal their 3D organization (Fig. 1 *b–d*). The axoneme is surrounded by a smooth and, in most regions, continuously visible plasma membrane (Fig. 1 *a*, *c*, and *d*). Only the upper and lower segments of the membrane fade out (e.g., top and bottom segments of membrane in Figs. 1*d* and 2); this fading out is due to the limited range of tilt angles (≈±65°) that is characteristic of ET ("missing wedge"). Note that the same is true for all image features that are oriented nearly perpendicular to the axis of the electron beam, including the walls of microtubules (Figs. 1*d*, 2, and 4*b*). The extracellular surface of the plasma membrane is decorated by one or two layers of densely packed particles

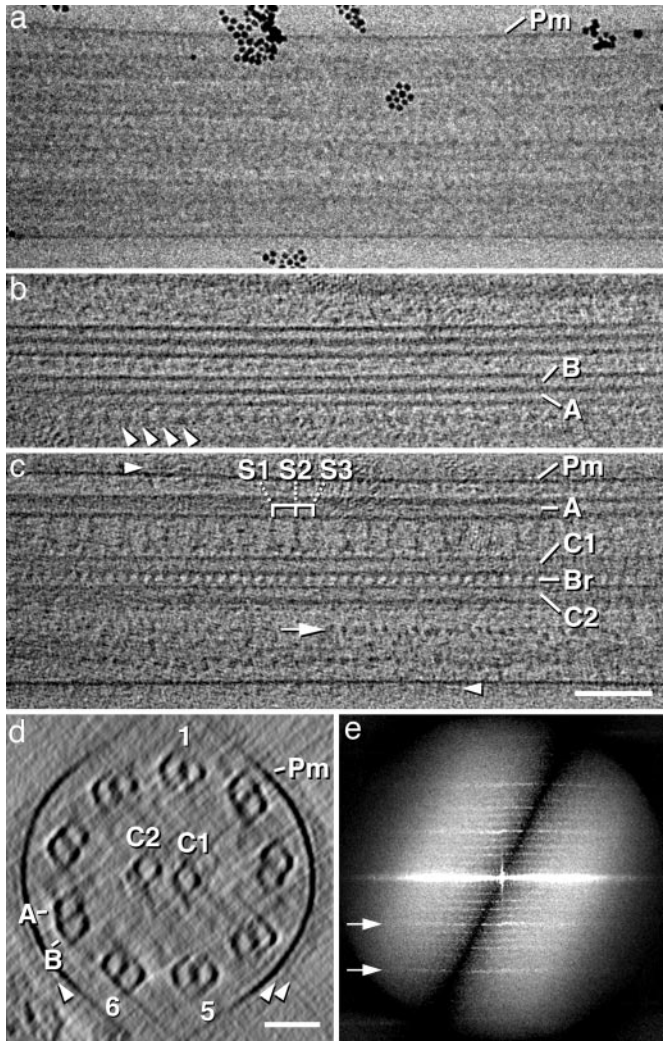

Fig. 1. Original electron micrograph and 3D reconstruction of a frozen-hydrated sea urchin sperm flagellum. (*a*) Transmission electron micrograph of an intact, quiescent, frozen-hydrated flagellum (dose of one electron per Å^2). In unstained frozen-hydrated specimens, protein appears dark, because it scatters electrons more than the surrounding solid water. Black spheres are 10-nm colloidal gold particles that are used as fiducial markers for alignment of the tilt series. (*b* and *c*) Approximately 20-nm-thick tomographic slices through the periphery (*b*) and the center (*c*) of the flagellum shown in *a* after 3D reconstruction. *b* shows a longitudinal view of two MTDs; note the row of ODAs (arrowheads). In *c*, two central singlet microtubules (C1 and C2) and the intermicrotubule bridges (Br) are seen. S1–S3, radial spoke triplets from proximal to distal; arrow, IDA densities; arrowheads, extracellular material at the plasma membrane (Pm). (*d*) Projection through ≈80 nm of the same tomogram as in *b* and *c*, but the slice is oriented perpendicular to the flagellar axis, showing the flagellum in cross section. The ring of MTDs (1/5/6), the central microtubule pair (C1 and C2), the plasma membrane (Pm), and the extracellular material at the plasma membrane (arrowheads) are evident, although horizontally oriented features fade out due to the missing wedge limitation. A and B mark the A and B tubules, which are the complete and incomplete cylinders, respectively. (*e*) Diffraction pattern of a 3D reconstruction of a frozen-hydrated flagellum; arrows mark the 1/16-nm (upper) and 1/8-nm (lower) layer lines. (Scale bars: *a–c*, 100 nm; *d*, 50 nm.)

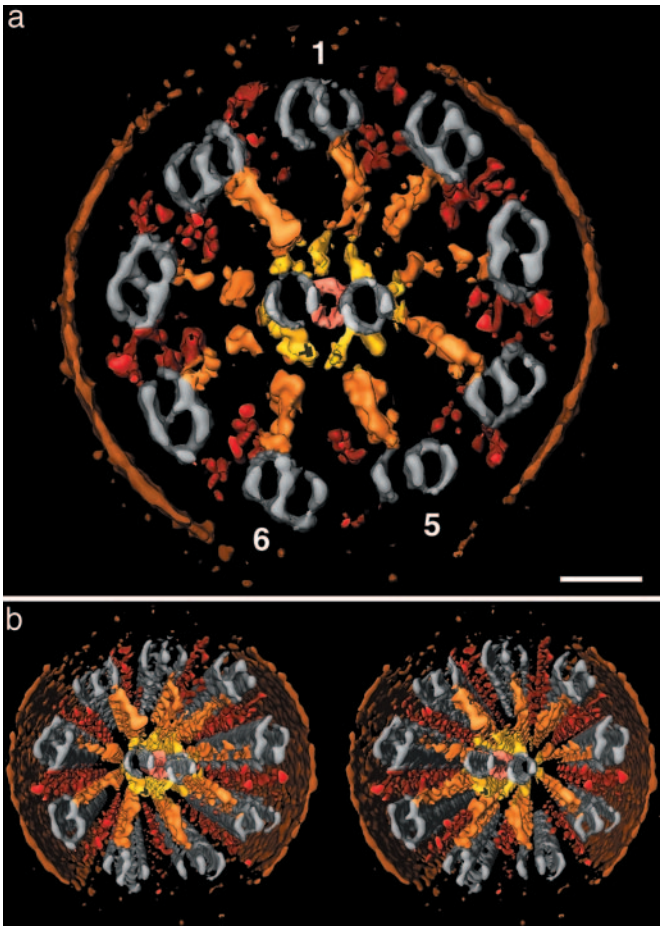

Fig. 2. Visualization of a 3D reconstructed sea urchin sperm flagellum. (*a* and *b*) Surface-rendered representations of a frozen-hydrated flagellum (same as in Fig. 1) in cross section; *b* shows a wall-eye stereo pair of *a*. The structures were translationally averaged using the 96-nm basic, axial periodicity, denoised, and then thresholded to identify the surfaces for display. Colors were applied to the following structures: plasma membrane (brown), microtubules (gray), ODAs and IDAs (red), radial spokes (orange), central pair protrusions (yellow), and bipartite bridges (pink). 1, 5, and 6 mark MTDs 1, 5, and 6. (Scale bar: 40 nm.)

(features just outside the dark line labeled Pm in Fig. 1 *a*, *c*, and *d* and marked with arrowheads in Fig. 1 *c* and *d*), whereas the cytoplasmic surface appears bare. The distance between the plasma membrane and the MTD is ≈20 nm and is relatively uniform. The axoneme itself has a diameter of ≈220 nm and displays the familiar "9 + 2" organization (Fig. 1 *c* and *d*). Extended views of the flagellum in longitudinal orientation never revealed deviations from a straight, untwisted organization (Figs. 1 *b* and *c* and 2*b*).

The axonemes have longitudinal periodicities, which are apparent in their diffraction pattern (Fig. 1*e*). The layer lines in the power spectra of the 3D reconstructions reflect fundamental periodicities along the flagellar axis. The most prominent periods are repeats at 8 and 16 nm (arrows) with lighter reflections that correspond, for example, to 96 nm (Fig. 1*e*). Still weaker reflections can sometimes be seen at higher frequencies, representing periodicity as small as 5.3 nm (not shown). Several macromolecular complexes that give rise to these patterns can readily be identified in the tomograms: (*i*) the radial spokes (Figs. 1*c*, 2, and 3*f*), (*ii*) the inner dynein arms (IDAs) and outer dynein arms (ODAs) (IDA, see arrow in Fig. 1*c*; ODA, Figs. 1*b*, 2, and 3 *a*–*c*), and (3) several structures associated with the central microtubule pair (Figs. 1 *c* and *d*, 2, and 4 *a*–*c*). The cross-sectional view of the flagellum shown in Fig. 2 displays the overall organization of the axoneme with impressive clarity. The radial spokes, the densities adjacent to the MTD that we interpret as the dynein arms, the central pair projections, and the central intermicrotubule bridges are all evident, particularly in the stereo pair (Fig. 2*b*).

Tomography Reveals Structural Features of the Dynein Arms. The IDAs originate close to the attachment sites of the radial spokes on the inner side of the A tubules, and we found several globular densities in this region (Figs. 1*c* and 2). The composition of the IDA is, however, complex (3, 5), and we could not clearly identify individual components. The ODAs, in contrast, are well defined and visible in both transverse and longitudinal slices through the MTD. Their attachments to the A tubule are more peripheral, and they repeat with a periodicity of 24 nm (Figs. 1*b*, 2, and 3 *a*, *b*, *d*, and *e*). The most prominent structures in each ODA complex are two ring-shaped heads that probably correspond to the heptameric motor domains of the dynein heavy chains (Figs. 2 and 3 *a*, *b*, *d*, and *e*). These features have previously been seen only in isolated dynein complexes (23–25). 3D correlation averaging of repeating ODAs has allowed us to improve the signal-to-noise ratio in the tomograms to visualize the heptameric ring *in situ* (Fig. 3*c*). These averaged images not only resolve individual dynein heads but also identify their orientation. The planes of the rings within each ODA complex are parallel to one another and to the plane that contains the longitudinal axes of the microtubules to which they are bound (Fig. 3 *a*, *b*, *d*, and *e*). Although both dynein heads of an ODA are about the same distance from the neighboring B tubule, the more peripheral head is further from the A tubule than its partner. The dynein stalks, which are thought to enable transient interaction with the adjacent B tubule (24), could not be visualized. The anchoring stem, also known as the tail, was also not unambiguously traceable. However, the mass densities distribution that was seen has led us to the interpretative diagrams depicted in Fig. 3 *d* and *e* (see *Discussion*).

The Radial Spokes Are Positioned with Bilateral Symmetry. The radial spokes associate with the A tubules between the attachment of the IDA and the junction of the A and B tubule (Fig. 2). The spoke shaft that projects from the A tubule wall toward the central pair complex (CPC) is ≈7 nm thick and 38–41 nm long, including the spoke head (Fig. 3*f*). The radial spokes are arranged in triplet groups with a repeat of ≈96 nm along each A tubule (Figs. 1*c* and 3*f*). The spacings between spokes are 32 nm (S1–S2), 24 nm (S2–S3), and 40 nm (S3–S1 of the next triplet). The spoke heads appear roughly triangular and are up to 20 nm wide (Fig. 3*f*). Analysis of the 3D arrangement of the radial spokes within straight axonemes revealed that the triplets from adjacent MTDs are longitudinally displaced (Fig. 3 *g*–*i*). However, unlike the helical pattern known from species such as *Tetrahymena* and *Chlamydomonas* (Fig. 3 *j* and *k*) (26), the radial spoke arrangement in sea urchin sperm flagella divides the axoneme into two hemicylinders that correspond to MTD 1–5 and MTD 6–1. The triplets of radial spokes are helically arranged on both sides of the axoneme, but the hands of the helices in the two hemicylinders are opposite (Fig. 3 *h* and *i*). An analysis of four different straight axonemes showed a bimodal distribution of shifts, with two peaks symmetrically distributed around zero at ≈±19 nm, instead of the single local maximum that would be expected for a continuous helix. This finding confirms our observation of two helically arranged hemicylinders with opposite handedness.

The Central Microtubules and Their Associated Materials Are also Positioned with a Symmetry That Anticipates the Form of the Flagellum's Beat. The two singlet microtubules of the CPC are connected by periodic bridges and surrounded by rows of projections

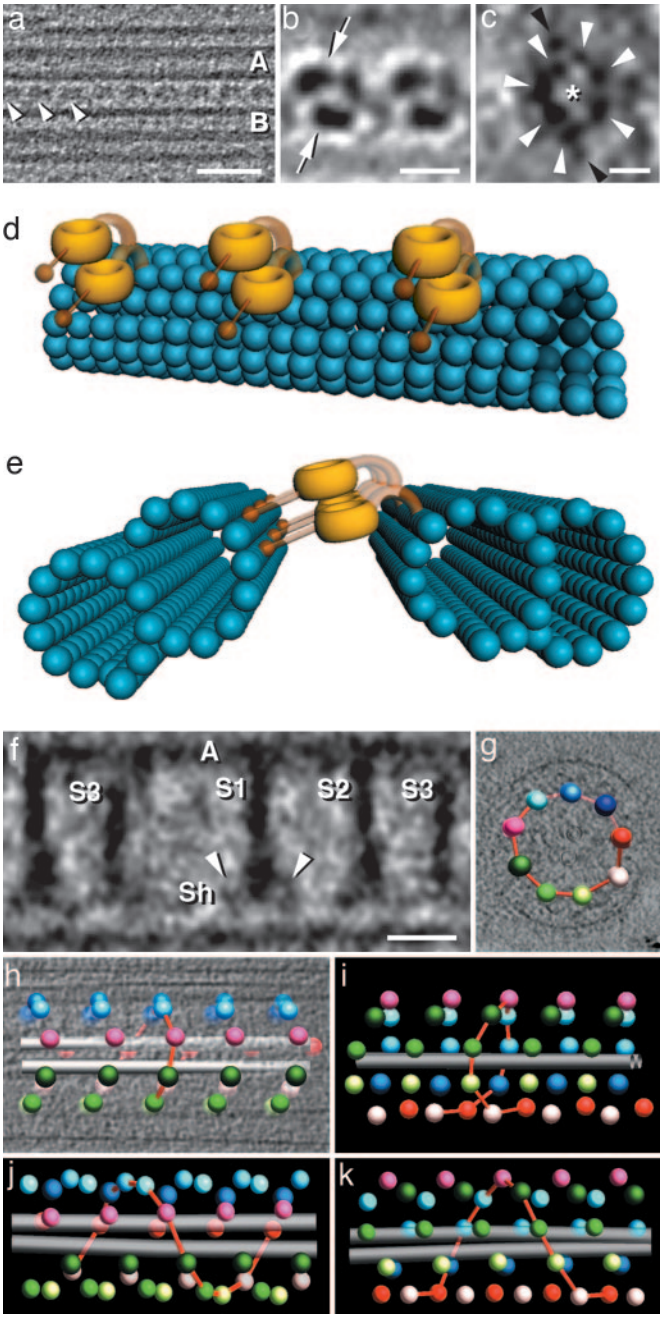

Fig. 3. Structural details and spatial arrangements of the ODAs and radial spokes. (*a*) Approximately 5-nm-thick tomographic slice showing a row of ODAs (arrowheads) that lies between two MTDs. The ODA periodicity is 24 nm; proximal is to the left; A and B mark the A and B tubules. (*b* and *c*) Averages of 20 ODA repeats. *b* shows the two dynein head domains (arrows) of two neighboring ODA complexes seen in a 2-nm-thick slice that contains the axis of the axoneme and cuts between adjacent MTDs. In *c*, the heptameric ring of a dynein head is shown. White arrowheads, seven subdomains surrounding a central cavity (asterisk); black arrowheads, two additional side domains. The orientation is similar to *a*, with the A-tubule-facing side at the top. (*d* and *e*) Interpretative diagrams showing the arrangement of the ODA (yellow) between two MTDs (blue); note that only the most medial dynein subunit (bottom) is directly attached to the A tubule (right side in *e*). Stems and stalks are displayed with transparency to indicate that their positions may be variable and are not certain. (*f*) Approximately10-nm-thick tomographic slice through an average of 36 repeats of radial spoke triplets (S1–S3). A, A tubule; Sh, spoke heads; arrowheads, two less dense lateral units. (*g–k*) Modeled representations of the bilaterally symmetric radial spoke arrangement in a sea urchin sperm flagellum (*g–i*) and helical arrangement seen in a *Tetrahymena* flagellum (*j* and *k*) (modeled after data from ref. 26). The spheres are positioned at the base of radial spoke S1, and each sphere represents a triplet; the red lines represent the shortest connections between triplets of neighboring MTDs and assist in recognizing the pattern of the radial spoke arrangement. In the cross section (*g*) and longitudinal representations (*h* and *i*) of the sea urchin, the colors are as follows. Pink shows radial spokes of doublet 1; the two bilateral symmetric halves are blue to red versus green to white; gray shows central microtubules. For better comparison, we used the same color scheme in *j* and *k*; however, these colored dots do not represent specific MTDs. (Scale bars: *a*, 50 nm; *b*, 15 nm; *c*, 5 nm; *f*, 20 nm.)

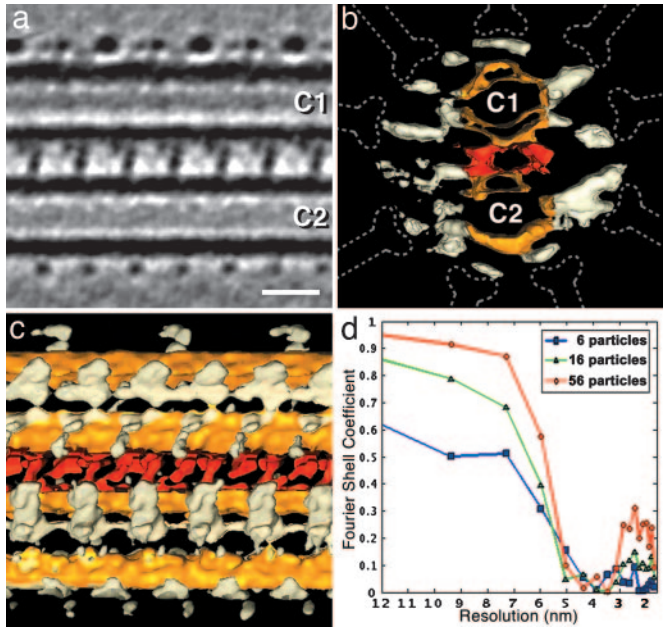

Fig. 4. Supramolecular structure of the CPC revealed by correlation averaging. (*a–c*) Average of 56 repeats of the CPC in longitudinal (*a* and *c*) and cross-sectional (*b*) view. In *a*, an ≈2-nm-thick tomographic slice is shown; in *b* and *c*, surface-rendered representations are shown. Colors were attributed as follows: yellow, central microtubules (C1 and C2); red, intermicrotubule bridges; white, central pair projections; dotted lines, position of radial spokes. The connections between the projections and the microtubules are not always continuously visible, depending on their orientation in relation to the missing wedge. Note the 32-nm repeat motif on the edge of C1 (top). In *a* and *c*, proximal is to the left. (*d*) Resolution evaluation for the CPC average shown in *a–c* obtained by calculating the Fourier shell correlation coefficient between separate averages that were created from either even- or odd-numbered particles. The resolution curves for increasing numbers of averaged particles (6, 16, and 56) clearly demonstrate the resolution improvement by correlation averaging. A Fourier shell correlation threshold of 0.5 provided a resolution estimate of ≈5.8 nm for the central region of the average. (Scale bar: 20 nm.)

that are in register along the flagellar axis (Figs. 1 *c* and *d*, 2, and 4 *a–c*). The projections are arranged with two principal repeat intervals along the microtubules: 16 nm for most of them; some shorter protrusions on the edge of the C1 microtubule form a meshwork with a 32-nm repeat (Fig. 4 *a* and *c*). The central microtubules are uniformly spaced by ≈12 nm. The intermicrotubule bridges have two branches and repeat at 16 nm (Figs. 1*c* and 4 *a–c*), and there are hints of additional material next to the bipartite bridges. We found at least 12 rows of projections from the central microtubules and some additional material arranged circumferentially around the CPC. The protrusions vary considerably in length, angle of projection, and shape (Fig. 4 *a–c*). However, there are two common themes: (*i*) All protrusions end on a cylinder with an ≈40-nm radius that is coaxial with the axoneme. The almost even distribution of protrusion endings matches very well the positions of the radial spoke heads, allowing close contact between the CPC protrusions and the

radial spokes (Fig. 4*b*). (*ii*) The set of protrusions connected to C1 appears approximately bilateral symmetric to the set bound to C2 (Fig. 4*b*). The two longest protrusions (toward MTD 5/6, right side in Fig. 4*b*) converge at a similar angle, whereas those on the opposite side run parallel. The plane of symmetry cuts between the two central microtubules and is almost identical to the aforementioned plane that parts the two hemicylinders of the radial spokes pattern. The only significant deviations from this apparent bilateral symmetry are the structures at the outer edge of the central microtubules, which repeat with either 16-nm (C2) or 32-nm (C1) periodicity. Using the 32-nm interval as a basic repeat unit, we aligned and averaged 56 CPC repeats. A resolution estimation using Fourier shell correlation indicated a resolving power better than 6 nm in this average (Fig. 4*d*).

Discussion

Cryo-electron tomography has several virtues as a method for studying cell structure. Rapid freezing without fixation or staining permits high confidence that the structures observed are preserved in a near-to-native state (27). Evidence of this good structural preservation is seen in the smooth appearance of the flagellar membrane, the uniform spacing between plasma membrane and axoneme, and the layer of material that covers the external surface of the membrane. The only structural descriptions of similar membrane-bound materials have come from other investigations of frozen-hydrated sea urchin sperm (11), suggesting that this structure can only be preserved by rapid freezing techniques. One of the major membrane proteins of the sea urchin sperm flagellum is the glycosylated receptor for egg jelly (REJ1) (28). Shedding of the extracellular domain from this protein might be a mechanism by which the flagellar membrane removes contaminants or achieves release from obstacles (29).

Our study by cryo-electron tomography has corroborated many previously described features of axoneme structure, such as periodicities and general organization (for reviews, see refs. 3, 5, and 7–9). More importantly, it has also provided insight into the macromolecular organization of this motile organelle. According to the diffraction patterns and the Fourier shell correlation of the CPC average, our tomograms contain structural information to a resolution better than 6 nm. In practice, however, features in this size range are often obscured by the low signal-to-noise ratio in cryo-tomograms. After 3D correlation averaging, however, features such as the heptameric ring and central cavity of the dynein heads became visible. Although this ring structure has been described previously at higher resolution (24, 25), it has previously been seen only in isolated dynein heavy chains. Here, we have visualized the domain structure of the ODA motor head in an intact flagellum, allowing us to describe its 3D orientation in relation to other structures. However, neither the stalks nor the stems could be resolved unambiguously in our data, which may indicate that they are flexible. Nonetheless, the positions of the ODA heads between the MTDs suggest that both dynein heavy chains could bind transiently to the B tubule by means of their stalks. Their positions also suggest that only the more inward-positioned dynein heavy chain is directly attached to the A tubule. We infer that the more outward-positioned dynein heavy chain might be carried piggyback by the inner subunit, possibly mediated by stem–stem interactions (see Fig. 3 *d* and *e*). Previously described cosedimentation and reconstitution experiments showed that sea urchin sperm flagella ODA binding to microtubules is mediated by the α-subunit (30). The combination of our observation with the latter report suggests that the more inward-positioned dynein heavy chain is the α-subunit. Analogous results have also been reported for the two-headed I1 IDA in *Chlamydomonas* (31).

Numerous structural and genetic studies have indicated that the radial spokes, the CPC, some dynein isoforms, and the dynein regulatory complex are all involved in the regulation of dynein activity and thus of microtubule sliding in active flagella (for reviews, see refs. 2 and 32–35). However, the mechanisms for the relevant signal transduction pathways are not well understood. The structural relationships among the players in this regulation are likely to be informative about how the system works (36–38). Our data provide previously unreported information about the spatial organization of the radial spokes and the CPC of sea urchin sperm flagella. We have found many correlations between the CPC of sea urchin sperm and *Chlamydomonas* flagella: e.g., the bipartite bridges, the additional material next to the bridges, the circumferential fibers, and the C1-edge projections that show 32-nm periodicity while all other microtubule-associated structures in the CPC repeat at 16-nm intervals (39, 40). Unlike the 7 rows of projections in *Chlamydomonas* (39), however, we found at least 12 rows that show a more symmetric arrangement than those described for the alga. Whereas the projections attached to one central microtubule are indeed asymmetrically arranged with different lengths and projection angles (compare the left and right sides of C1 or C2), the distributions from C1 and C2 look alike and show an approximate bilateral symmetry. It seems also that the CPC protrusions, which all terminate on a cylinder that surrounds the axoneme's axis, represent a well defined "adapter system" between the radially symmetric spoke system and the bilaterally symmetric singlet microtubules. In the future, the analysis of frozen-hydrated axonemes of *Chlamydomonas* and other species could show whether the different numbers of CPC projections are species-specific, related to the bending pattern of the axoneme, or the result of different preparation techniques.

A close relationship between radial spokes and the CPC is also reflected by the symmetries that divide the axoneme into two halves (MTDs 1–5 and 6–1). Although it is not yet clear whether this symmetry will turn out to be widely distributed or a species/cell-type-specific feature, we propose that it relates to the form of the flagellar beat. The waveform of beating sea urchin sperm flagella is mainly planar; quasi-planar and helical waveforms were rarely observed [e.g., only when the flagellum was subjected to an environment of increased viscosity (41)]. To produce a planar wave, the dynein arms on one side of the axoneme should be active while those on the other side are inactive and able to allow passive microtubule sliding in a direction opposite to that of their own power stroke (42). The CPC in sea urchin sperm flagella maintains a fixed orientation relative to the bending plane (7). Therefore, microtubule sliding needs to oscillate between the two hemicylinders that contain MTDs 2–5 and 7–9. The orientation of the symmetry plane relative to that of the planar wave is consistent with a regulation model in which dynein activity switches between the two hemicylinders to produce flagellar strokes in opposite directions, as suggested in earlier studies of sea urchin axonemes (43).

The notion that the CPC and the radial spokes are important for the regulation of the flagellar waveform is not new (7, 35). Our data, however, inform this debate by showing a correlation between bilateral symmetry of the internal flagellar structures and the waveform of sea urchin sperm flagella. We propose that the geometric arrangements of axonemal components play crucial roles in the function of the regulatory system that controls axonemal motility and generates the characteristic waveforms. In this context, it is interesting to compare the architecture of the sea urchin sperm flagellum with analogous structures in the axonemes of organisms like *Chlamydomonas*, where the flagellar waveform is more complex. Differences in the macromolecular composition and in spatial arrangement of axoneme components (e.g., the absence of an S3 radial spoke and the rotating CPC in *Chlamydomonas*) (26) coincide nicely with the fundamentally different waveforms of these flagella. Although the radial spoke system and CPC are not essential for axonemal motility *per se*, their interactions may be important for controlling the size and

shape of the waveforms that can be altered in response to specific stimuli (35, 40). For instance, the symmetry of axonemal bends is often modified by changes in the calcium concentration of the surrounding medium (44).

The present work extends previous studies in several ways: (*i*) ET has solved the problem of structural superposition (11), (*ii*) the use of frozen-hydrated flagella has preserved near-to-native structure and doubled the resolution in comparison with ET of plastic embedded flagella (12), (*iii*) the axonemes described here were not compressed, and (*iv*) unlike the studies of isolated flagellar components, the macromolecular complexes were maintained in their cellular context. We have established a basis for further studies both to identify individual components by labeling and mutant comparison and to investigate functional dynein motor enzymes *in situ*. 3D reconstructions of different functional states of the flagellar beat trapped by rapid freezing should allow us to study the molecular mechanism of actively beating flagella with considerable accuracy in four dimensions, thereby characterizing the structural changes that dynein undergoes during its mechanochemical cycle.

We thank Rick Gaudette, David Mastronarde, and Friedrich Foerster for help with the image processing. We are grateful to Mary Porter for critically reading the manuscript and to Win Sale and Victor Vacquier for helpful comments. This work was supported by a Max-Planck Forschungspreis (to W.B.), the Fonds der Chemie (W.B.), and National Institutes of Health Grant RR00592 (to J.R.M.).

1. Silflow, C. D. & Lefebvre, P. A. (2001) *Plant Physiol.* **127,** 1500–1507.
2. Porter, M. E. & Sale, W. S. (2000) *J. Cell Biol.* **151,** F37–F42.
3. Mitchell, D. R. (2000) *J. Phycol.* **36,** 261–273.
4. Mitchell, D. R. (1994) *Int. Rev. Cytol.* **155,** 141–180.
5. Porter, M. E. (1996) *Curr. Opin. Cell Biol.* **8,** 10–17.
6. Karki, S. & Holzbaur, E. L. (1999) *Curr. Opin. Cell Biol.* **11,** 45–53.
7. Gibbons, I. R. (1981) *J. Cell Biol.* **91,** 107s–124s.
8. Satir, P. (1984) *J. Protozool.* **31,** 8–12.
9. Snell, W. J., Pan, J. & Wang, Q. (2004) *Cell* **117,** 693–697.
10. Murray, J. M. (1994) *Curr. Opin. Struct. Biol.* **4,** 180–186.
11. Murray, J. M. (1986) *J. Ultrastruct. Mol. Struct. Res.* **95,** 196–209.
12. McEwen, B. F., Radermacher, M., Rieder, C. L. & Frank, J. (1986) *Proc. Natl. Acad. Sci. USA* **83,** 9040–9044.
13. Frank, J. (1992) *Electron Tomography: Three-Dimensional Imaging with the Transmission Electron Microscope* (Plenum, New York).
14. Koster, A. J., Grimm, R., Typke, D., Hegerl, R., Stoschek, A., Walz, J. & Baumeister, W. (1997) *J. Struct. Biol.* **120,** 276–308.
15. Taylor, K. A. & Glaeser, R. M. (1974) *Science* **186,** 1036–1037.
16. Dubochet, J., Adrian, M., Chang, J. J., Homo, J. C., Lepault, J., McDowall, A. W. & Schultz, P. (1988) *Q. Rev. Biophys.* **21,** 129–228.
17. Gibbons, B. H. (1982) *Methods Cell Biol.* **25,** 253–271.
18. Gatti, J. L. & Christen, R. (1985) *J. Biol. Chem.* **260,** 7599–7602.
19. Hegerl, R. (1996) *J. Struct. Biol.* **116,** 30–34.
20. Walz, J., Typke, D., Nitsch, M., Koster, A. J., Hegerl, R. & Baumeister, W. (1997) *J. Struct. Biol.* **120,** 387–395.
21. Frangakis, A. S. & Hegerl, R. (2001) *J. Struct. Biol.* **135,** 239–250.
22. Kremer, J. R., Mastronarde, D. N. & McIntosh, J. R. (1996) *J. Struct. Biol.* **116,** 71–76.
23. Samso, M., Radermacher, M., Frank, J. & Koonce, M. P. (1998) *J. Mol. Biol.* **276,** 927–937.
24. Burgess, S. A., Walker, M. L., Sakakibara, H., Knight, P. J. & Oiwa, K. (2003) *Nature* **421,** 715–718.
25. Samso, M. & Koonce, M. P. (2004) *J. Mol. Biol.* **340,** 1059–1072.
26. Goodenough, U. W. & Heuser, J. E. (1985) *J. Cell Biol.* **100,** 2008–2018.
27. Dubochet, J. & Sartori Blanc, N. (2001) *Micron* **32,** 91–99.
28. Moy, G. W., Mendoza, L. M., Schulz, J. R., Swanson, W. J., Glabe, C. G. & Vacquier, V. D. (1996) *J. Cell Biol.* **133,** 809–817.
29. Trimmer, J. S. & Vacquier, V. D. (1988) *Exp. Cell Res.* **175,** 37–51.
30. Moss, A. G., Sale, W. S., Fox, L. A. & Witman, G. B. (1992) *J. Cell Biol.* **118,** 1189–1200.
31. Perrone, C. A., Myster, S. H., Bower, R., O'Toole, E. T. & Porter, M. E. (2000) *Mol. Biol. Cell* **11,** 2297–2313.
32. Curry, A. M. & Rosenbaum, J. L. (1993) *Cell Motil. Cytoskeleton* **24,** 224–232.
33. Habermacher, G. & Sale, W. S. (1996) *J. Cell Sci.* **109,** 1899–1907.
34. Smith, E. F. & Lefebvre, P. A. (1997) *Cell Motil. Cytoskeleton* **38,** 1–8.
35. Smith, E. F. & Yang, P. (2004) *Cell Motil. Cytoskeleton* **57,** 8–17.
36. Diener, D. R., Curry, A. M., Johnson, K. A., Williams, B. D., Lefebvre, P. A., Kindle, K. L. & Rosenbaum, J. L. (1990) *Proc. Natl. Acad. Sci. USA* **87,** 5739–5743.
37. Dutcher, S. K. (2000) *J. Eukaryot. Microbiol.* **47,** 340–349.
38. Huang, B., Piperno, G., Ramanis, Z. & Luck, D. J. (1981) *J. Cell Biol.* **88,** 80–88.
39. Mitchell, D. R. & Sale, W. S. (1999) *J. Cell Biol.* **144,** 293–304.
40. Mitchell, D. R. (2003) *Cell Motil. Cytoskeleton* **55,** 188–199.
41. Woolley, D. M. & Vernon, G. G. (2001) *J. Exp. Biol.* **204,** 1333–1345.
42. Brokaw, C. J. (1991) *J. Cell Biol.* **114,** 1201–1215.
43. Sale, W. S. (1986) *J. Cell Biol.* **102,** 2042–2052.
44. Hosokawa, Y. & Miki-Noumura, T. (1987) *J. Cell Biol.* **105,** 1297–1301.